Structures 68 (2024) 107266

Contents lists available at ScienceDirect

Structures

journal homepage: www.elsevier.com/locate/structures

Behavior of cross-shaped stiffened concrete-filled steel tubular stub columns after fire exposure

Weiwei Wang [a], Xuetao Lyu [b,*], Xin Liu [b], Jun Zheng [a], Han Gao [c], Yang Yu [c,d,**]

[a] School of Architectural Engineering, Guangzhou Vocational and Technical University of Science and Technology, Guangzhou 510000, China
[b] School of Transportation and Civil Engineering, Foshan University of Science and Technology, Foshan 528231, China
[c] Centre for Infrastructure Engineering and Safety, School of Civil and Environmental Engineering, The University of New South Wales, Sydney, NSW 2052, Australia
[d] Multidisciplinary Center for Infrastructure Engineering, Shenyang University of Technology, Shenyang 110870, China

ARTICLE INFO

Keywords:
Post fire
Cross shaped reinforced concrete-filled steel tubular stub columns
Axial compression

ABSTRACT

The cross-shaped stiffened concrete-filled steel tubular stub column is constructed by incorporating steel reinforcement ribs into the traditional cross-shaped design, which helps delay the buckling of the steel tube and enhances its restraining effect on the concrete. However, existing standards and research proposed design methods for estimating the post-fire bearing capacity of steel reinforced concrete stub columns are primarily applicable to the ordinary steel tubes with conventional thickness and sections. Therefore, it is necessary to investigate the axial compressive properties of high-strength concrete stub columns with irregular thin-walled steel tubes after exposure to fire, which can contribute to their potential future application. Effects of various experimental parameters, such as heating time, width-thickness ratio, and longitudinal spacing of stiffeners were investigated. In total one specimen subjected to ambient temperature and eight cross-shaped stiffened concrete-filled steel tubular stub columns subjected to fire conditions were prepared for measuring temperature-time curves of specimens during ISO-834 standard fire, load-displacement curves, load-transverse, and longitudinal strain curves of specimens under axial compression loading. The failure modes of the specimens were recorded, and the influence of each parameter on the post-fire mechanical properties of the specimens was analyzed based on the experimental results. ABAQUS software was utilized to develop a model for post-fire analysis, which was validated by comparing it with experimental data. After validation, the model was used to analyze the underlying mechanism, and a comprehensive parametric study of members was conducted. Based on the results of the parametric study and the model developed for calculating bearing capacity of the cross-shaped stiffened concrete-filled steel tube stub column at ambient temperature, a simplified equation accounting for the effects of elevated temperature was proposed to predict the residual bearing capacity of the cross-shaped stiffened concrete-filled steel tube stub column after fire exposure. The average error between the simplified formula and the finite element simulation results is 0.925, and the mean square error is 0.085.

1. Introduction

The concrete-filled steel tube column is a composite structure formed by using steel tube as a template filled with concrete [1], combining the advantages of both steel tube and concrete [2–8]. In comparison to traditional cross-sections (circular, square, and rectangular), specially shaped columns (T-, L-, or cross-shaped) can circumvent the impact of protruding corners on the house space, thereby enhancing the utilization of interior space. Consequently, special-shaped columns find extensive use in building structures [9–11].

However, the mechanical properties of special-shaped columns differ significantly from those of traditional columns due to the increased restraint effect of steel tubes on the corners compared to the middle of the section. In other words, the distribution of the restraint effect across the entire component is uneven [12,13]. Additionally, while the use of thin-walled steel tubes reduces the amount of steel required, these tubes may experience premature local buckling, thereby diminishing the constraint effect on the core concrete. This, in turn, hinders the full

* Corresponding author.
** Corresponding author at: Centre for Infrastructure Engineering and Safety, School of Civil and Environmental Engineering, The University of New South Wales, Sydney, NSW 2052, Australia.
E-mail addresses: lxtwww30@fosu.edu.cn (X. Lyu), yang.yu12@unsw.edu.au (Y. Yu).

https://doi.org/10.1016/j.istruc.2024.107266
Received 12 March 2024; Received in revised form 20 August 2024; Accepted 9 September 2024
Available online 12 September 2024

realization of the interaction between the steel tubes and concrete, ultimately resulting in a reduction in bearing capacity [14–17].

The restraining effect of steel tubes on concrete can be achieved by using stiffeners to prevent or delay local buckling of thin-walled steel tubes. Previous literature has proposed several forms of reinforcement, such as steel plates [18], bound steel bars [19,20], tensile reinforcement ribs [21–24] and shear connectors [25]. The findings from the research indicate that incorporation of stiffeners can enhance the bearing capacity by 6–53 % and increase ductility by 54–650 %. However, the above research only focuses on the performance of special-shaped steel tube concrete columns under ambient temperature conditions.

Fire can degrade the material properties of steel and concrete, thereby affecting the bearing capacity and stiffness of members and structures. During a fire, steel structures are susceptible to collapse [26], and high-strength concrete columns may spall when exposed to high temperatures [27]. However, due to the low thermal conductivity and high heat capacity of concrete, as well as the steel tube protecting the core concrete from cracking, the failure probability of CFST after fire is relatively low. Therefore, it is crucial to evaluate the residual performance of damaged structures after exposure to fire for renovation and reuse [28]. Studies on circular, square and rectangular CFST under fire and after fire have been widely reported, such as circular steel-reinforced CFST columns [29,30], square steel-reinforced CFST columns [31], square steel tube confined reinforced concrete columns [32], square concrete columns [33], and rectangular CFST columns. However, due to the variation in cross-sectional shape leading to different mechanical behaviors, these results cannot be directly applied to special-shaped CFST columns.

The literature review highlights a significant research gap regarding the mechanical properties of special-shaped steel tube concrete columns following fire exposure, particularly due to the lack of research on the post-fire mechanical properties of this new type of composite column. In light of this, key experimental variables such as, width-to-thickness ratio, heating time, and the longitudinal spacing of stiffeners were selected in this study, which was informed by the research results previously reported by our team [34–38]. Consequently, temperature heating and cooling tests along with axial compression tests on cross-shaped stiffened concrete-filled steel tubular (CSCFST) stub columns were performed to investigate these effects. Using ABAQUS software, the temperature field model and the mechanical analysis model were established and validated through comparison with experimental test results. The residual bearing capacity was analyzed based on parameters such as heating time, longitudinal spacing of stiffeners, section size, and material strengths. Consequently, a simplified formula for calculating residual bearing capacity was developed.

2. Experimental program

2.1. Test specimens

Nine CSCFST stub columns axial compression test specimens, and seven temperature measurement specimens were designed. The design parameters of the specimens are shown in Table 1, and the cross-sectional dimensions are shown in Fig. 1. The main parameters of the test are the heating time t_h (0 min, 45 min, 90 min), width-to-thickness ratio (width-to-thickness ratio = limb width/thickness of the steel tube, 45, 60, 90), and the longitudinal spacing S between stiffeners (without stiffener, 50 mm, 100 mm)..

2.2. Mechanical properties of materials

To measure the material properties of the steel tube, tensile coupons were performed following GB/T 228.1–2010 (GB/T, 2010) [39]. The average results of the mechanical properties of the structural steel are reported in Table 2, including the yield stress f_y, the ultimate stress f_u, Young's modulus E_s and the Poisson ratio μ_s, and δ_s is percentage elongation at fracture. Properties of steel reinforcement were also tested according to GB/T 228.1–2010 (GB/T, 2010) [39], and the results are shown in Table 3, including the yield stress f_{yb}, the ultimate stress f_{ub}, Young's modulus E_{sb}, and the percentage elongation after fracture δ_{sb}.

The compressive strength and elastic modulus of concrete were tested using 150 mm cubes and 150 mm × 150 mm × 300 mm prisms respectively in accordance with GB/T50081–2002 (GB/T, 2002) [40]. The results are presented in Table 4, which contains the average

Table 1
Design parameters of the specimens.

No.	a_1 ×a_2 ×b_1 ×b_2 ×h× t_s ×H mm×mm×mm×mm× mm×mm	d×S mm×mm	width-to-thickness ratio	t_h min
DS100 −60 −0	60 × 60 × 60 × 60 × 180 × 3 × 540	6 × 100	60	0
DS0 −60 −45	60 × 60 × 60 × 60 × 180 × 3 × 540	-	60	45
DS100 −90 −45	60 × 60 × 60 × 60 × 180 × 2 × 540	6 × 100	90	45
DS100 −60 −45	60 × 60 × 60 × 60 × 180 × 3 × 540	6 × 100	60	45
DS100 −45 −45	60 × 60 × 60 × 60 × 180 × 4 × 540	6 × 100	45	45
DS50 −90 −45	60 × 60 × 60 × 60 × 180 × 2 × 540	6 × 50	90	45
DS50 −60 −45	60 × 60 × 60 × 60 × 180 × 3 × 540	6 × 50	60	45
DS50 −45 −45	60 × 60 × 60 × 60 × 180 × 4 × 540	6 × 50	45	45
DS100 −60 −90	60 × 60 × 60 × 60 × 180 × 3 × 540	6 × 100	60	90
T100 − 90 −45	60 × 60 × 60 × 60 × 180 × 2 × 540	6 × 100	90	45
T100 − 60 −45	60 × 60 × 60 × 60 × 180 × 3 × 540	6 × 100	60	45
T100 − 45 −45	60 × 60 × 60 × 60 × 180 × 4 × 540	6 × 100	45	45
T50 − 90 −45	60 × 60 × 60 × 60 × 180 × 2 × 540	6 × 50	90	45
T50 − 60 −45	60 × 60 × 60 × 60 × 180 × 3 × 540	6 × 50	60	45
T50 − 45 −45	60 × 60 × 60 × 60 × 180 × 4 × 540	6 × 50	45	45
T100 − 60 −90	60 × 60 × 60 × 60 × 180 × 3 × 540	6 × 100	60	90

Note: 1. Naming principle of the specimen: the letters "DS" and "T" denote the specimens for axial compression test and temperature measurement respectively; the first number indicates stiffener spacing (e.g. "0" means no reinforcement stiffeners are present). The second number represents width-to-thickness ratio, the third number corresponds to heating time. 2. a_1 , a_2 , b_1 , b_2 and h correspond to the sizes of the cross section; t_s is steel tube thickness, and H *is* column length, d is stiffener's diameter.

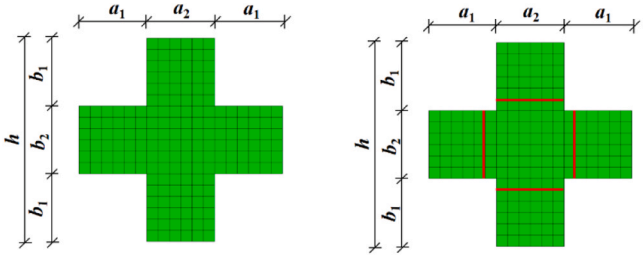

Fig. 1. Cross-sectional view of the specimens.

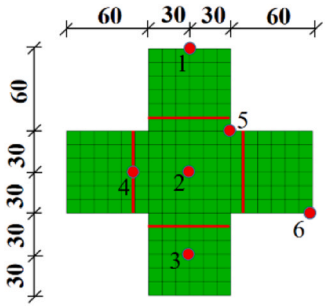

Fig. 2. Temperature measure points.

Table 2
Material properties of steel tube.

t_h (min)	t_s (mm)	f_y (N/mm^2)	f_u (N/mm^2)	E_s ($\times 10^5$ N/mm^2)	μ_s	δ_s (%)
0 min	2.89	229.88	318.03	1.89	0.34	37.34
45 min	1.92	196.34	314.07	1.83	0.36	36.04
90 min	2.64	195.22	311.18	1.65	0.31	32.87

Table 3
Material properties of steel reinforcement.

d (mm)	f_{yb} (N/mm^2)	f_{ub} (N/mm^2)	E_{sb} ($\times 10^5$ N/mm^2)	δ_{sb} (%)
6.00	283.01	397.95	1.67	15.77

Table 4
Material properties of concrete.

Grade	$f_{cu,28d}$/ (N/mm^2)	$f_{cu,test}$/ (N/mm^2)	E_c ($\times 10^5$ N/mm^2)	v_c	moisture content
C30	30.5	38.0	0.28	0.18	4.29 %

compressive strength of concrete cubes after a curing period of 28 days $f_{cu,28d}$, the compressive strength on the day the specimens were tested $f_{cu,test}$, the elastic modulus E_c, and the Poisson's ratio v_c. The moisture content was also tested following GB/T20313–2006 (GB/T, 2006) [41].

2.3. Test equipment and procedure

The experimental procedure consists of two primary phases: the heating test and the subsequent compression test. The test instruments consist of a multifunctional fire test furnace, a 200-ton hydraulic compression testing machine, Agilent temperature acquisition instrument and dynamic signal acquisition instrument, etc. (Fig. 3).

The main test stages are as follows: 1) The specimens were placed in the furnace in 3 batches as shown in Fig. 4, which were underwent a heating regimen conforming to the ISO 834 standard fire curve including both the heating and cooling phases. 2)After cooling to ambient temperature, these specimens were subjected to compression until failure to obtain failure patterns and load-displacement curves.

multifunctional fire test furnace hydraulic compression testing machine

Fig. 3. testing equipment.

3. Test observations and results

3.1. Heating test

Fig. 5 illustrates the observable changes on the exterior surface of the steel tube after exposure to fire for specimens DS100–60-0 (unheated), DS100–60-45 (subjected to 45 min of heating), and DS100–60-90 (subjected to 45 min of heating), respectively. From the figure, it can be seen that the surface of the steel tube heated for 45 mins exhibited a significant "crispy" oxide layer, with a notable diminution in metallic sheen relative to the unfired specimens; the specimen exposed to 90 min of heating displayed a formation of reddish-brown oxide layer at the edges, and the outer surface of the tube show extensive areas of flaking and detachment.

Fig. 6 shows the comparison between the measured temperature of the fire test furnace and the rise and fall curve of ISO-834 standard. It can be seen that the temperature in the fire test furnace is in good agreement with the standard rise and drop curve, and the test furnace can accurately provide the fire environment of the components..

Temperature-time curves for critical points within these specimens throughout the entire heating and cooling cycle are shown in At approximately 100 ℃, transient plateau in the heating curve of concrete is observed, which is because the evaporation and migration of water inside the concrete carry away most of the heat, stabilizing the

Fig. 4. The position of the specimen.

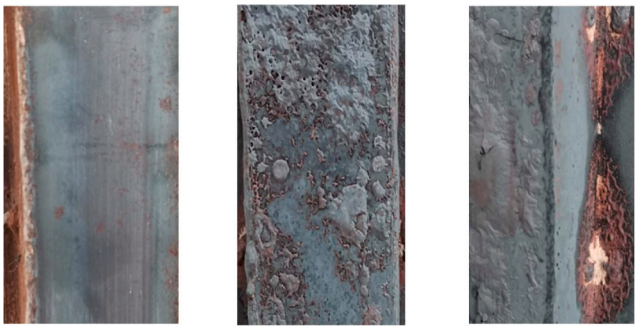

(a)Unfired (b)Heating time 45min (c)Heating time 90min

Fig. 5. Appearance of the steel tube on the exposed surface.

temperature of the concrete for a certain period of time. After the water evaporates, the temperature of the concrete continues to rise. Steel has a higher rate of heating and higher historical peak temperatures that can be reached than concrete, due to the higher thermal conductivity of steel compared to concrete, which is characterized by heat transfer hysteresis and high heat absorption capacity.

The specimen heated for 90 min can reach a higher historical maximum temperature than the specimen heated for 45 min, and the temperature at the center of the concrete is the lowest compared to other positions. The temperature changes at the internal and external corners of the steel tube, as well as at the middle position of the surface, are basically consistent. With the changes in width to thickness ratio and spacing between steel reinforcement ribs, there is no significant difference in the overall temperature changes of the specimen, indicating that it has little effect on the heat transfer effect of the component.

3.2. Axial compression test

3.2.1. Experimental phenomena

Fig. 8 illustrates the numbering of each side of the stub specimens and the observed changes of the specimens at the end of the loading phase. To facilitate the observation, the cross section of each specimen is numbered from 1 to 12. Generally, for an axially compressed specimen, when the load reaches approximately 40 % of the peak load, the sound of slightly broken concrete began to be heard; As the load progresses to around 60 % of the peak load, the oxidized layer of some test specimens was slightly peeled off. When reaching about 85 % of the peak load, the steel tube started to bulge slightly, followed by the sound of cracking concrete. When the load reached to 95 % of the peak load, the number of local bulges gradually increased, and the extent of bulges progressively intensified until it reached the peak load. When the load drops to 80–70 % peak load, stop loading and end the test.

3.2.2. Compression test results

3.2.2.1. Typical failure modes. Fig. 9 shows the typical failure patterns of the specimens. The figure shows that the failure mode of concrete is mainly longitudinal crushing failure. The internal concrete of the specimen subjected to 90 min of heating exhibits a higher degree of looseness, and more pronounced crushing, which is due to the intensification of concrete deterioration at elevated temperature; There are different degrees of bulging on all sides of the specimens, mainly concentrated in the middle of the specimens. The specimen with a spacing of 50 mm between stiffeners has more bulging, and the longer the heating time, the more obvious the degree of bulging.

3.2.2.2. Load-displacement curves. In order to analyze the effects of spacing between stiffeners, width-to-thickness ratio, and heating time on the mechanical properties of members after fire exposure, axial compression tests were conducted. The load-displacement curve of the specimens was measured as shown in Fig. 10, and the yield displacements of the specimens were obtained through geometric plotting method. The residual bearing capacity, axial compression stiffness, ductility and other mechanical properties of the specimen are shown in Table 5.

The yield displacements of the specimens (Δ_y) were obtained using geometric plotting method, as shown in Fig. 11. First, tangent line OA is drawn through the origin O, and a horizontal line AU is drawn over the peak load point U. Point A is determined by the intersection of OA and AU. A straight-line AB, parallel to the *N* axis, passes through point A, and intersects the load-displacement curve at point B. Extend OB to intersect with AU at point C. A line CY is drawn parallel to the N axis, which intersects the load-displacement curve at point Y. Point Y is the yield point of the specimen, and Δ_y is the yield displacement of the specimen. Point P is the displacement $\Delta_{0.85}$ corresponding to 0.85 times the peak load in the load-displacement decreasing section. The ductility coefficient μ is the ratio of $\Delta_{0.85}$ to Δ_y. The axial compressive stiffness *EA* is the product of the elastic modulus of the combined section E_{sc} and the section area A_{sc}. E_{sc} is the secant modulus corresponding to 0.4 times the peak load in the load-displacement curve. The residual bearing capacity (N_{uT}), axial compression stiffness (*EA*), ductility and other mechanical properties of the specimen are shown in Table 5.

3.2.2.3. Load-strain curves

3.2.2.3.1. Load-longitudinal strain. Fig. 12 shows the load-longitudinal strain relationship curves of CSCFST stub columns. The longitudinal strain of the specimen, with 'positive' and 'negative' values indicating tensile and compressive strains respectively, mainly reflects the local changes in the middle position of the specimen. Due to issues such as the adhesion of strain gauges, some data points were not captured during the test phase.

From Fig. 12, it can be seen that during the initial loading stage of the

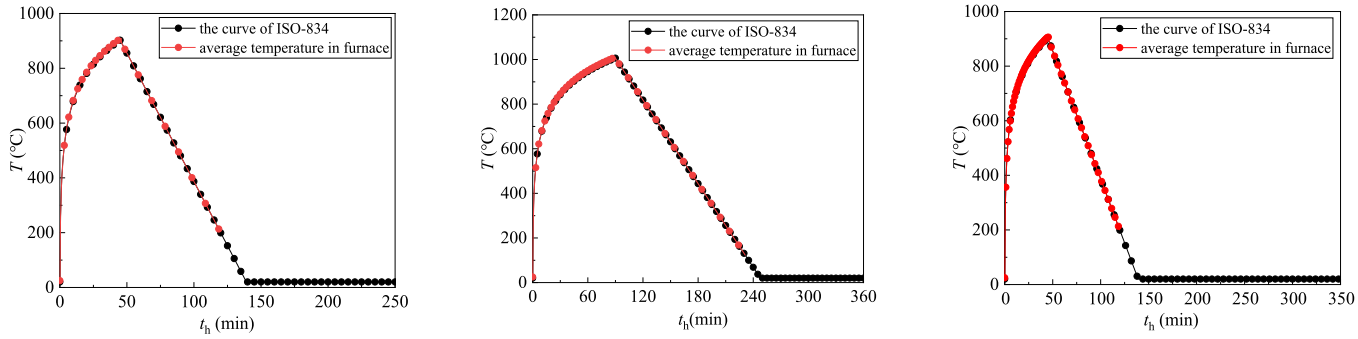

(a)The first furnace specimen (b)The second furnace specimen (c)The third furnace specimen

Fig. 6. Comparison of furnace temperature rise and drop curve with ISO-834 standard.

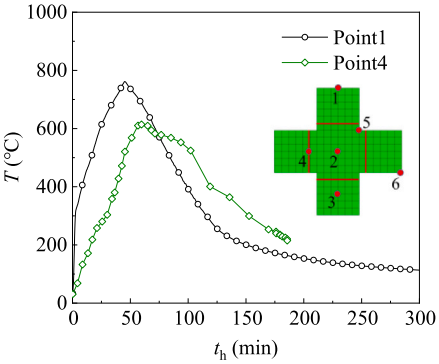

(a)T100-90-45

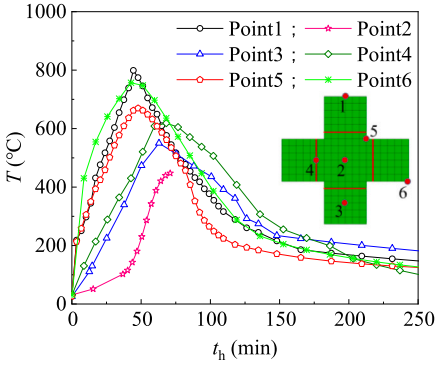

(b)T100-60-45

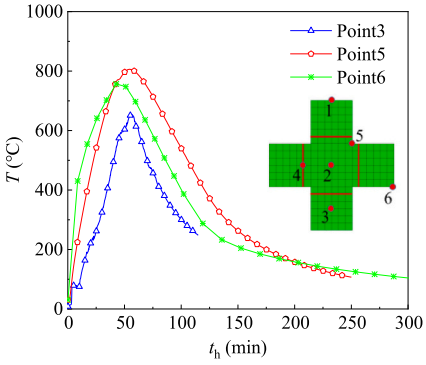

(c)T100-45-45

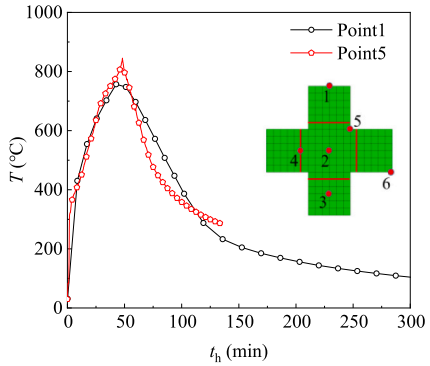

(d)T50-90-45

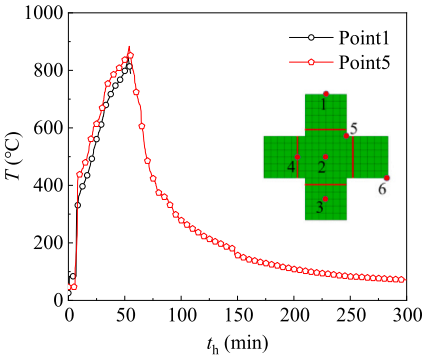

(e)T50-60-45

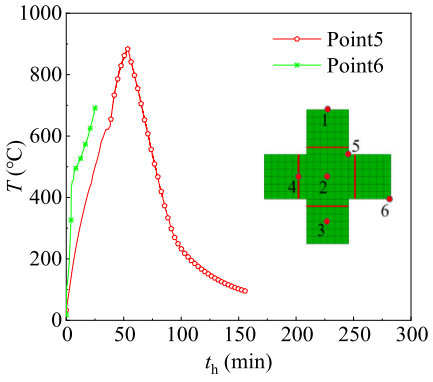

(f)T50-45-45

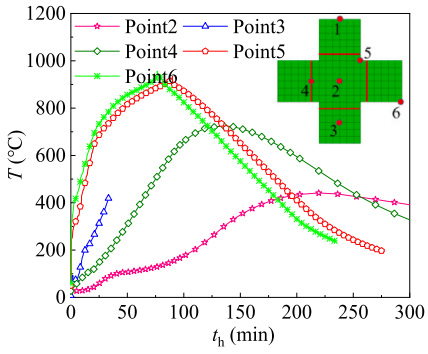

(g)T100-60-90

Fig. 7. Specimen temperature-time curve.

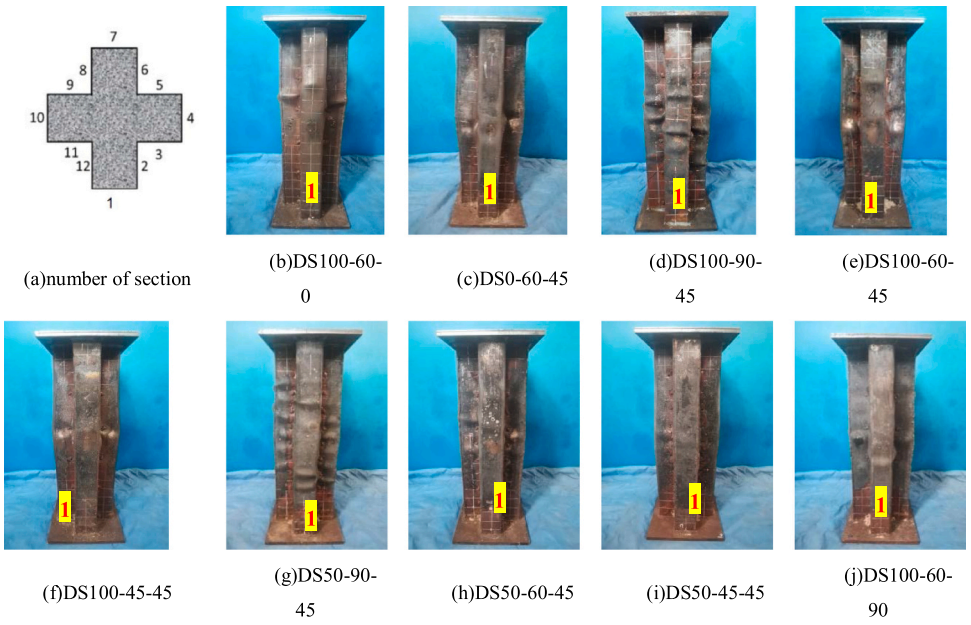

Fig. 8. Surface numbers and failure mode of the tested specimens.

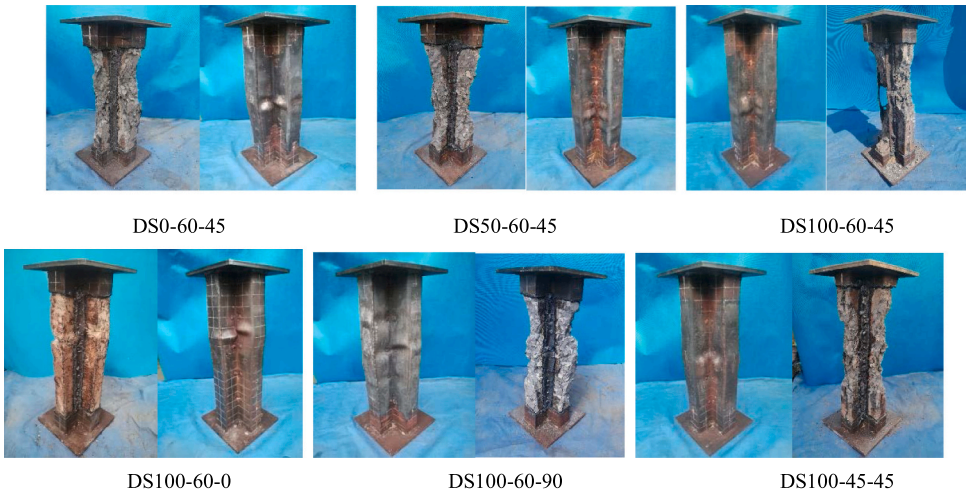

Fig. 9. Typical failure modes.

specimen, the load longitudinal strain curve of the specimen shows a linear growth trend, and with the continuous increase of the specimen load, the strain of the steel tube increases rapidly into a nonlinear growth stage due to the localized bulging of the steel tube. The maximum strain on the 7–12 side of the specimen DS0–60-45 exceeds 20000με, the maximum strain on the 6, 8–10, and 12 side of specimen DS100–60-45 is about 15000με, the maximum strain on 5–6 side of specimen DS50–60-45 is 10000με nearby.

Compared to specimens without stiffeners, the addition of stiffeners effectively inhibits the buckling of the steel tube, resulting in a slower rate of longitudinal strain development. Moreover, the smaller the spacing between stiffeners, the smaller the strain value of the specimen. The strain value of specimen DS50–45-45 is smaller than that of specimen DS50–60-45 because the thicker the steel tube results in less bulging under load, leading to a lower strain value. The strain value of specimen DS100–60-0, which was not subjected to fire, increased very slightly in the early stages of loading. After the load reached its peak, the strain increased rapidly. Compared to specimens heated for 45 min and 90 min, the strain increased significantly in the early stages of loading, and the increase was far greater than that of unfired specimens. After reaching the peak load, the strain value began to decline gradually. This is because compared to unfired specimens, the increased heating time causes the steel tube of the fire exposed specimen to reach yield earlier.

3.2.2.3.2. Load-transversal strain. Fig. 13 shows the load-transversal strain relationship curves of CSCFST stub columns. The transversal strain of the specimen, with 'positive' values indicating tensile strain and 'negative' values indicating compressive strains, mainly reflects the lateral constraint ability of the steel tube on the core concrete. Due to the adhesion issues with strain gauges as well as other factors, some data is missing during the test process.

From the figure, it can be seen that the load-transversal strain of the specimen shows a linear growth trend in the early stage of loading. As local bulging of the specimen appears, the transversal strain of the specimen gradually increases. The strain values on the 1 and 7 side of specimen DS100–60-45, are smaller than those on the 2, 9, and 12 side. This indicates that the steel tube exerts a greater constraint effect on concrete near the anodized corner than near the shaded corner. The strain growth rate of specimens DS100–60-45 with a spacing of 100 mm between stiffeners slows down after reaching peak load on sides 1, 3, 6–8, 10, and 11. This can be attributed to the addition of stiffeners,

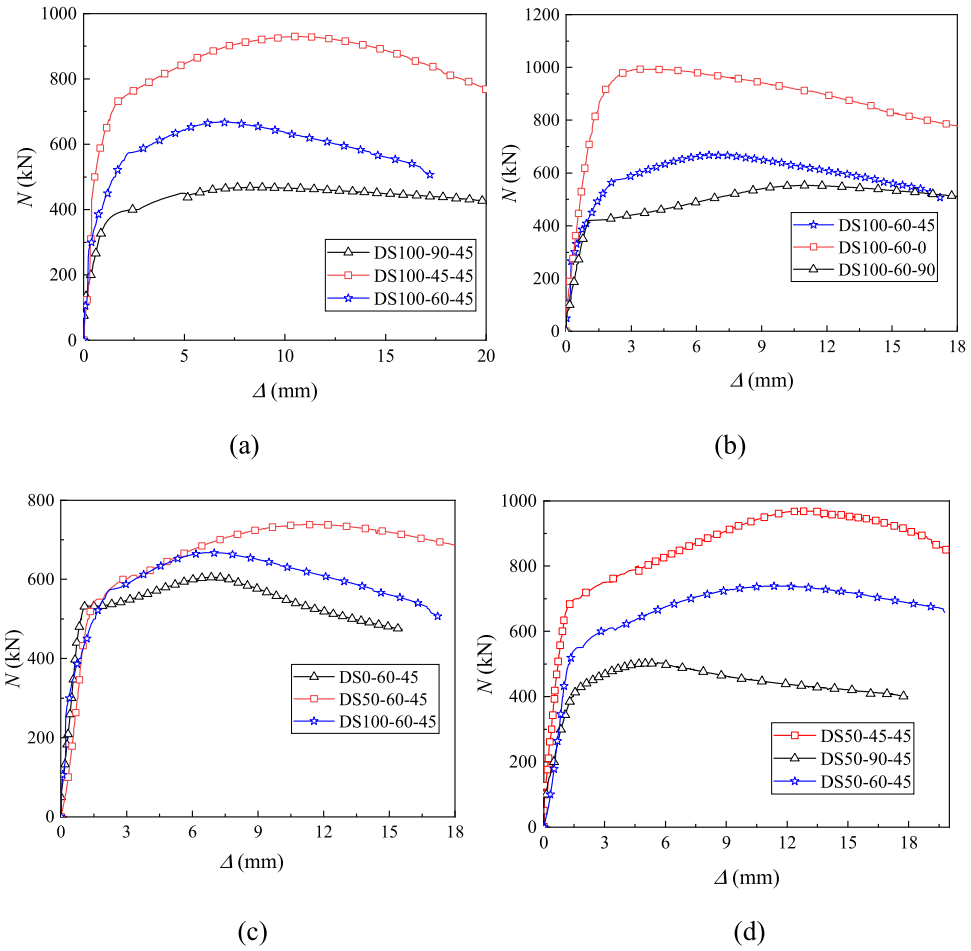

Fig. 10. Load-displacement curves.

Table 5
Mechanical properties of specimens.

No.	N_{uT} (kN)	EA ($\times 10^5$ kN)	Δ_y (mm)	$\Delta_{0.85}$ (mm)	μ
DS100 −60 −0	993.55	3.88	1.47	14.22	9.67
DS0 −60 −45	605.09	2.24	2.61	12.31	4.72
DS100 −90 −45	468.13	1.90	2.62	20.26	7.73
DS100 −60 −45	668.13	2.31	1.47	14.53	9.88
DS100 −45 −45	929.25	3.53	1.87	19.21	10.27
DS50 −90 −45	501.27	1.99	1.76	14.14	8.03
DS50 −60 −45	739.23	2.34	2.24	22.58	10.08
DS50 −45 −45	968.21	3.86	1.71	21.93	12.82
DS100 −60 −90	552.48	2.25	1.02	NA	NA

which effectively improve the restraining effect of steel tube on concrete, suppress further local buckling of steel tube, and prevent further strain development.

The strain increase of the unfired specimens during the initial loading stage is very small, and it only begins to develop rapidly after reaching the peak load. In contrast, the strain of specimens subjected to fire begins to develop rapidly before reaching the peak load, indicating that high temperature leads to earlier circumferential confinement of steel tube on concrete. The strain values of specimens DS50–45-45 are smaller than those of specimens DS50–90-45 and DS50–60-45, indicating that as the width-to-thickness ratio decreases, the transversal confinement effect of the steel tube becomes stronger.

4. Finite element analysis

ABAQUS is used to establish the finite element model of temperature field and mechanical analysis.

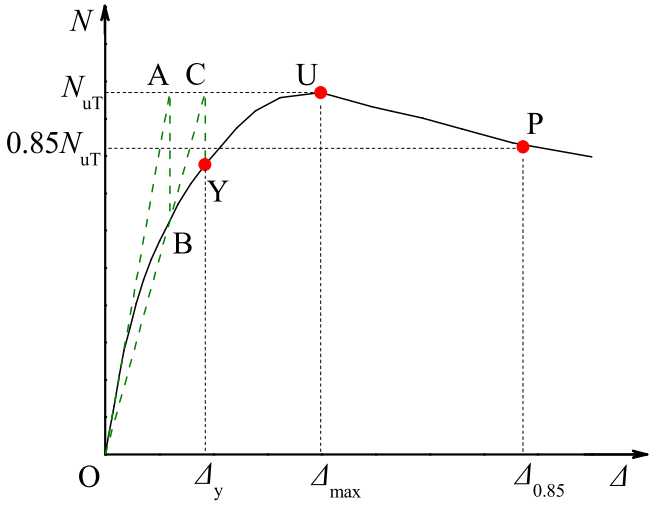

Fig. 11. Determination of yield displacement.

4.1. Verification of temperature field model

The material densities are recommended by the European specification EC4 [42] with the density of steel tubes and steel bars ρ_s and ρ_b taken as 7850 kg/m^3 and concrete density ρ_c taken as 2300 kg/m^3. The

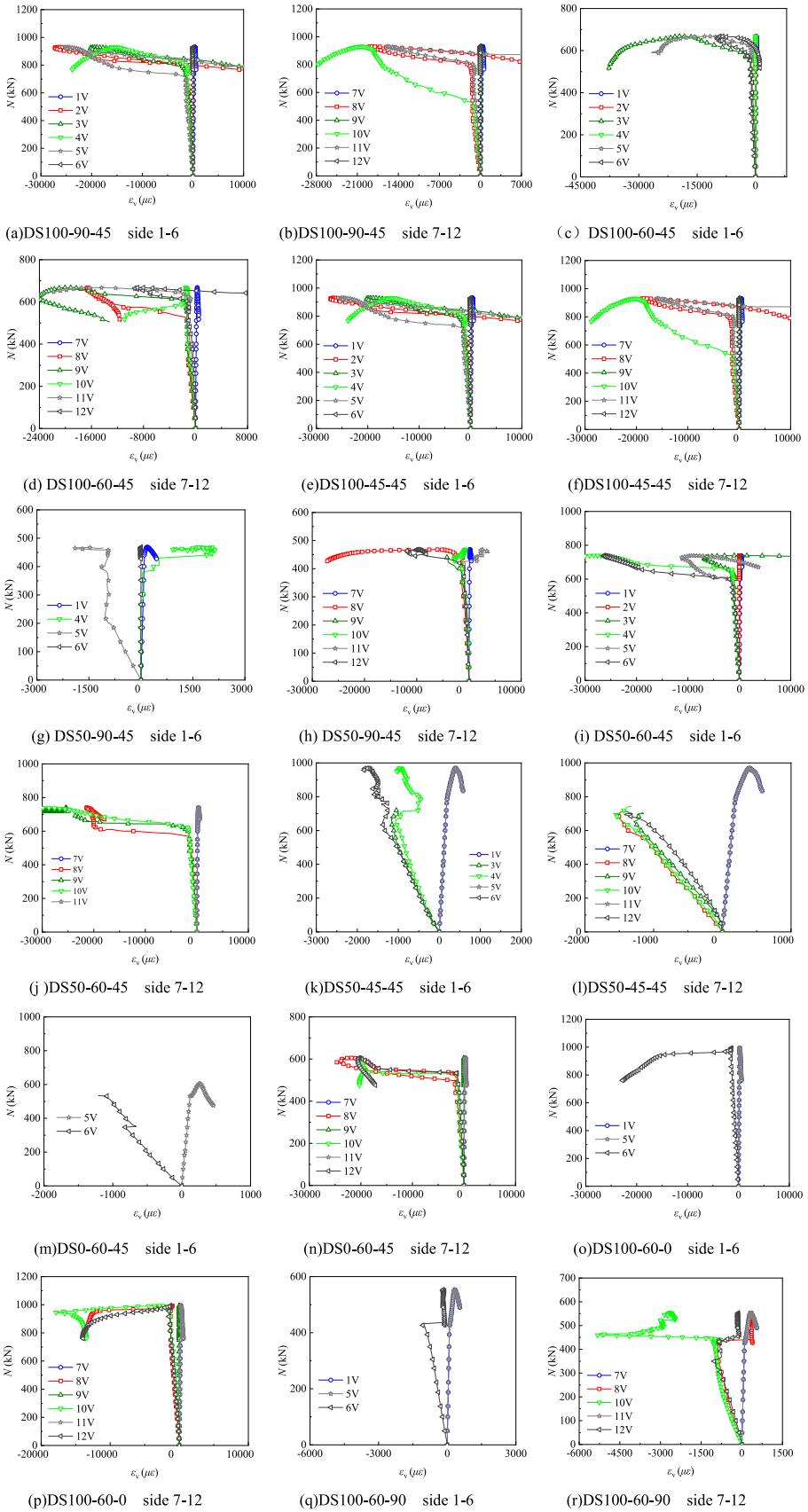

(a)DS100-90-45 side 1-6 (b)DS100-90-45 side 7-12 (c) DS100-60-45 side 1-6

(d) DS100-60-45 side 7-12 (e)DS100-45-45 side 1-6 (f)DS100-45-45 side 7-12

(g) DS50-90-45 side 1-6 (h) DS50-90-45 side 7-12 (i) DS50-60-45 side 1-6

(j)DS50-60-45 side 7-12 (k)DS50-45-45 side 1-6 (l)DS50-45-45 side 7-12

(m)DS0-60-45 side 1-6 (n)DS0-60-45 side 7-12 (o)DS100-60-0 side 1-6

(p)DS100-60-0 side 7-12 (q)DS100-60-90 side 1-6 (r)DS100-60-90 side 7-12

Fig. 12. Load-longitudinal strain relation curves.

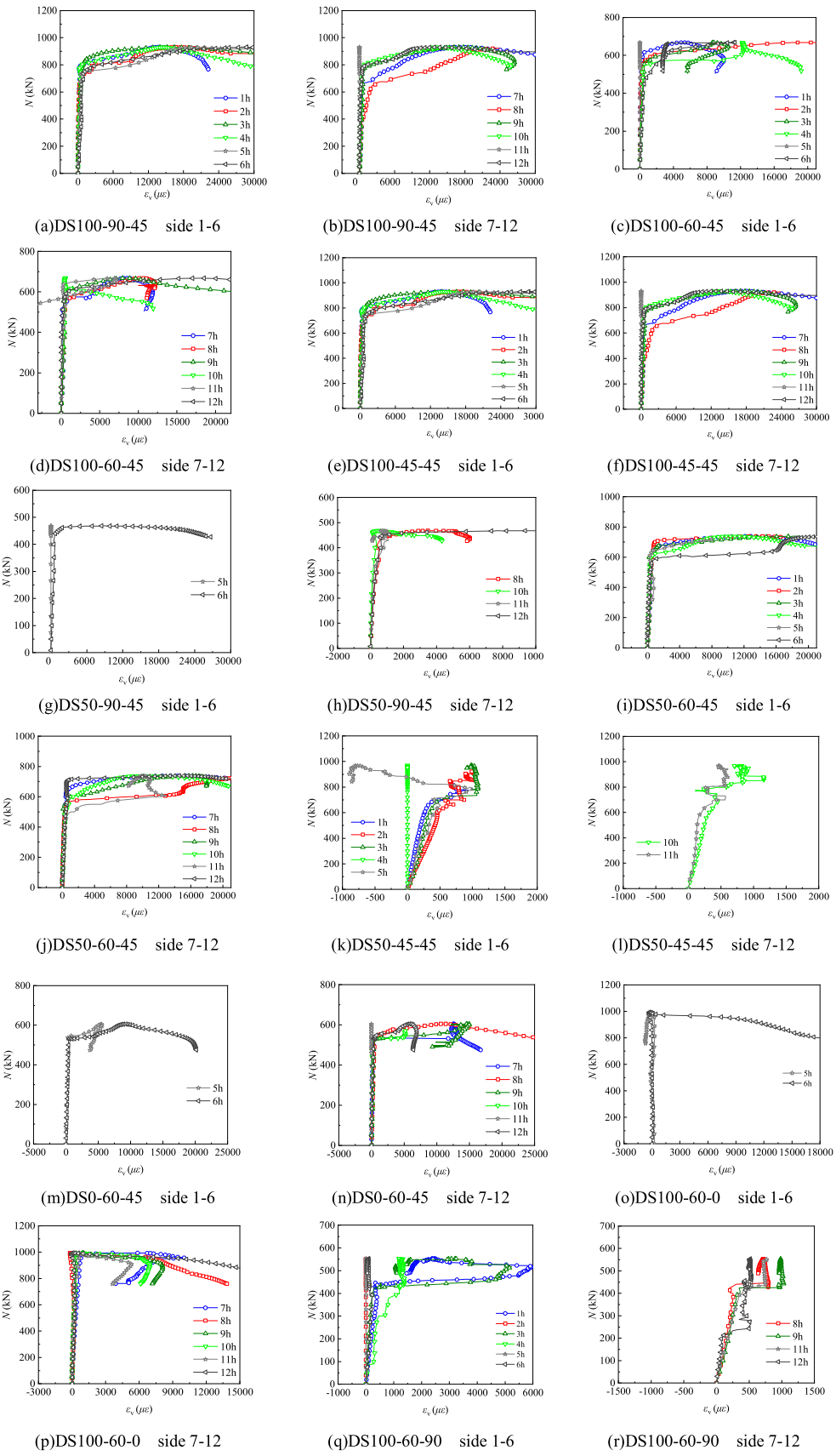

(a)DS100-90-45 side 1-6 (b)DS100-90-45 side 7-12 (c)DS100-60-45 side 1-6

(d)DS100-60-45 side 7-12 (e)DS100-45-45 side 1-6 (f)DS100-45-45 side 7-12

(g)DS50-90-45 side 1-6 (h)DS50-90-45 side 7-12 (i)DS50-60-45 side 1-6

(j)DS50-60-45 side 7-12 (k)DS50-45-45 side 1-6 (l)DS50-45-45 side 7-12

(m)DS0-60-45 side 1-6 (n)DS0-60-45 side 7-12 (o)DS100-60-0 side 1-6

(p)DS100-60-0 side 7-12 (q)DS100-60-90 side 1-6 (r)DS100-60-90 side 7-12

Fig. 13. Load-lateral strain relation curves.

thermal conductivity, as well as the specific heat of concrete and steel, are recommended according to EC4 [42]. The analysis step of the temperature field is set as "heat transfer". To account for the temperature hysteresis effect of concrete during the heat transfer process, the duration of analysis step is set to be greater than the total duration of the heating and cooling time in the temperature field model. According to the European standard EC4 [42], thermal convection and radiation are determined, with a comprehensive thermal radiation coefficient of 0.7 and a convective heat transfer coefficient of 25 W/(m^2·℃). The ISO-834 standard rising and cooling curves are imported into the finite element software as amplitude curves. The Boltzmann constant is set to $5.67\bullet10^{-8}$ W/(m^2 K^4), absolute zero is set to −273 ℃, and a predefined field is created with an initial ambient temperature of 20 ℃.

The inner surface of the steel tube and the outer surface of the concrete are set as surface-to-surface contact (Surface to Surface), with the concrete surface designated as the master surface and the steel tube surface set as the slave surface. Due to the thermal expansion and contraction of the concrete, a gap formed between the concrete and the steel tube. The contact thermal resistance is set to 0.01(m^2·℃)/W [43]. The stiffeners are embedded in concrete and tied to the inner surface of the steel tube. A four-node thermal analysis shell unit (DS4) is used for steel tube, and eight-node three-dimensional thermal analysis solid unit (DC3D8) is used for concrete. Furthermore, two-node heat transfer linear rod unit (DC1D2) is used for steel reinforcement. Structural mesh technology is used, and to ensure the accuracy of the model calculation, the spacing between the seeds is set to 10 mm.

Fig. 14 shows the comparison between the calculated results of the finite element model and the measured data of the temperature field. A close correlation between these two sets of data is observed, affirming that this model can accurately reflect the temperature changes experienced by the specimen under fire conditions.

4.2. Verification of mechanical analysis model

The elastic modulus of the steel tube is taken as 200,000 MPa at ambient temperature and its value after exposing to elevated temperature is determined according to the findings from literature [44]. The stress-strain relationship is defined using the secondary plastic flow model:

$$\sigma_s = \begin{cases} E_s\varepsilon_s & \varepsilon_s \le \varepsilon_e \\ -A\varepsilon_s^2 + B\varepsilon_s + C & \varepsilon_e < \varepsilon_s \le \varepsilon_{e1} \\ f_y & \varepsilon_{e1} < \varepsilon_s \le \varepsilon_{e2} \\ f_y[1 + 0.6(\varepsilon_s - \varepsilon_{e2})/(\varepsilon_{s3} - \varepsilon_{e2})] & \varepsilon_{e2} < \varepsilon_s \le \varepsilon_{e3} \\ 1.6\,f_y & \varepsilon_s > \varepsilon_{e3} \end{cases} \quad (1)$$

where , $\varepsilon_e = 0.8f_y/E_s$, $\varepsilon_{e1} = 1.5\varepsilon_e$, $\varepsilon_{e2} = 10\varepsilon_{e1}$, $\varepsilon_{e3} = 100\varepsilon_{e1}$; $A = 0.2f_y/(\varepsilon_{e1}\text{-}\varepsilon_e)^2$, $B = 2A\varepsilon_{e1}$, $C = 0.8f_y + A\varepsilon_e^2\text{-}B\varepsilon_e$.

The elastic modulus of steel stiffeners at room temperature and after exposing to high temperature is consistent with that of steel tubes. The stress-strain of steel bars is modeled using an ideal elastic-plastic model. The yield strength after high temperature is determined according to reference [44]. At room temperature, the elastic modulus of concrete is

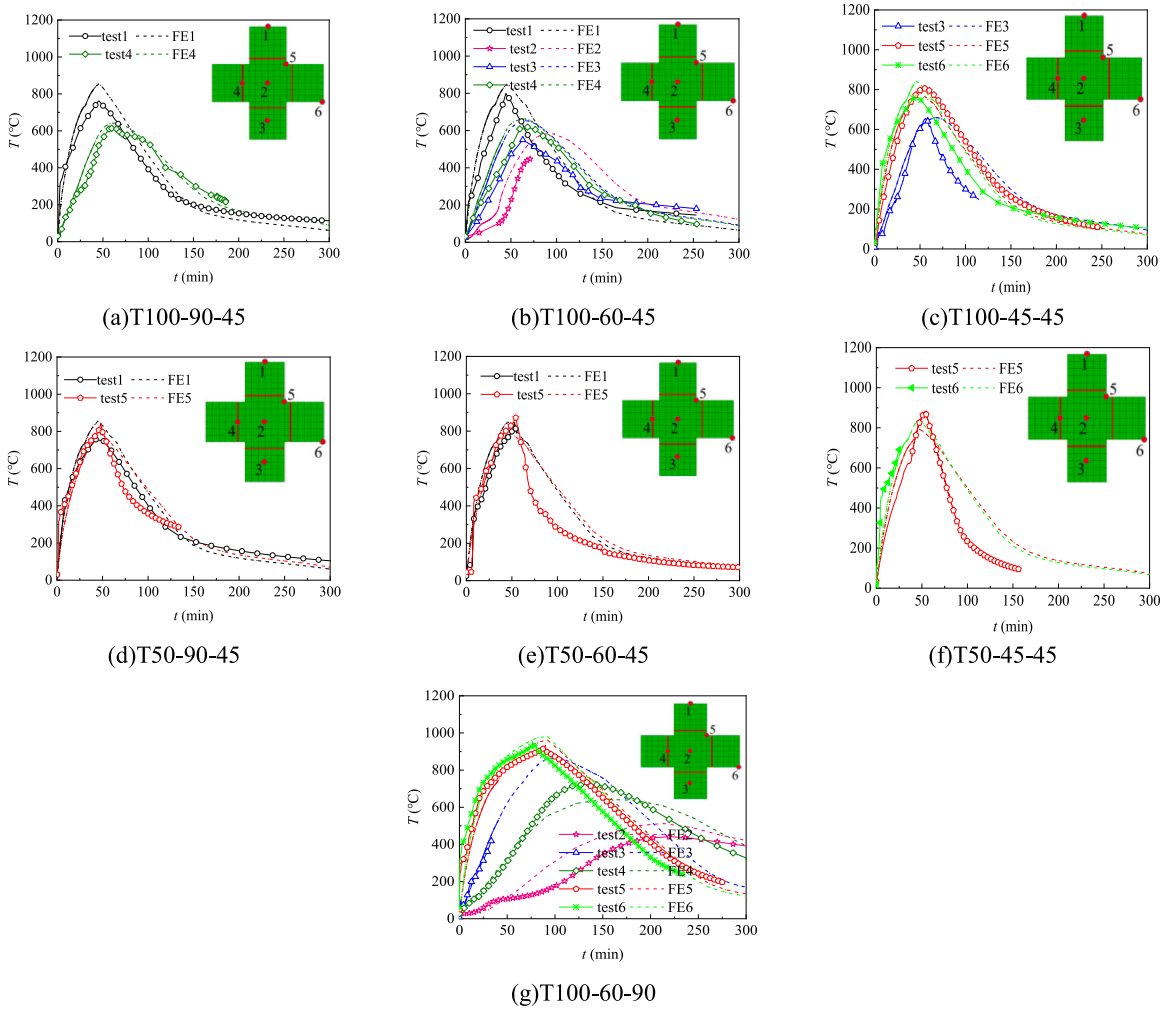

Fig. 14. Comparison and verification of temperature field and finite element model.

selected based on the recommended value of ACI 318 (2011) [45], and after high temperature, the formula recommended by Xie [46] is used. The compressive stress-strain relationship of concrete follows the recommendations in literature [47], while the tensile stress strain relationship is based on literature [48].

The node temperature data file is calculated through the temperature analysis step and imported into the corresponding nodes of the mechanical analysis model through the written Fortran subroutine [49]. Then a static analysis step is conducted of the mechanical performance of the member by applying displacement loads and improves the convergence of the model by setting the energy dissipation fraction.

The inner surface of the steel tube and the outer surface of the concrete are set to surface-to-surface contact, with hard contact in the normal direction and Coulomb friction model in the tangential direction. The friction coefficient is set to 0.6 at room temperature and 0.3 after fire exposure [49]. Tie constraints are set between steel stiffeners and steel tubes, and embedded regions are used between steel stiffeners and concrete. The degrees of freedom for U1, U2, UR1, UR2, and UR3 at the upper end face of the members are restricted, while the lower end face is completely fixed and loaded by displacement with a loading step of 1 % of the column length. C3D8R, S4R, and T3D2 are respectively used for concrete, steel tubes and steel stiffeners. The mesh division of the mechanical analysis model is consistent with the temperature field model.

Fig. 15 shows the comparison between the measured load-displacement curves and the finite element simulation results. The overall correlation between the observed data and the simulated results is notably strong, although there is a deviation in the stiffness simulation of a few specimens during the elastic stage. This deviation may be attributed to the influence of non-dense concrete pouring and welding between the reinforcing steel stiffeners and steel tubes during the specimen preparation process.

Fig. 16 also presents both experimental and numerical simulation results of the failure modes of the specimens, demonstrating that they are in good agreement.

5. Parametric analysis and design method

To further study the mechanical properties of members after fire, the parameters such as heating time t_h, concrete compressive strength f_{cu}, steel tube yield strength f_y, steel stiffener rib yield strength f_{yb}, steel tube thickness t_s, limb thickness b, section size h/b and the longitudinal

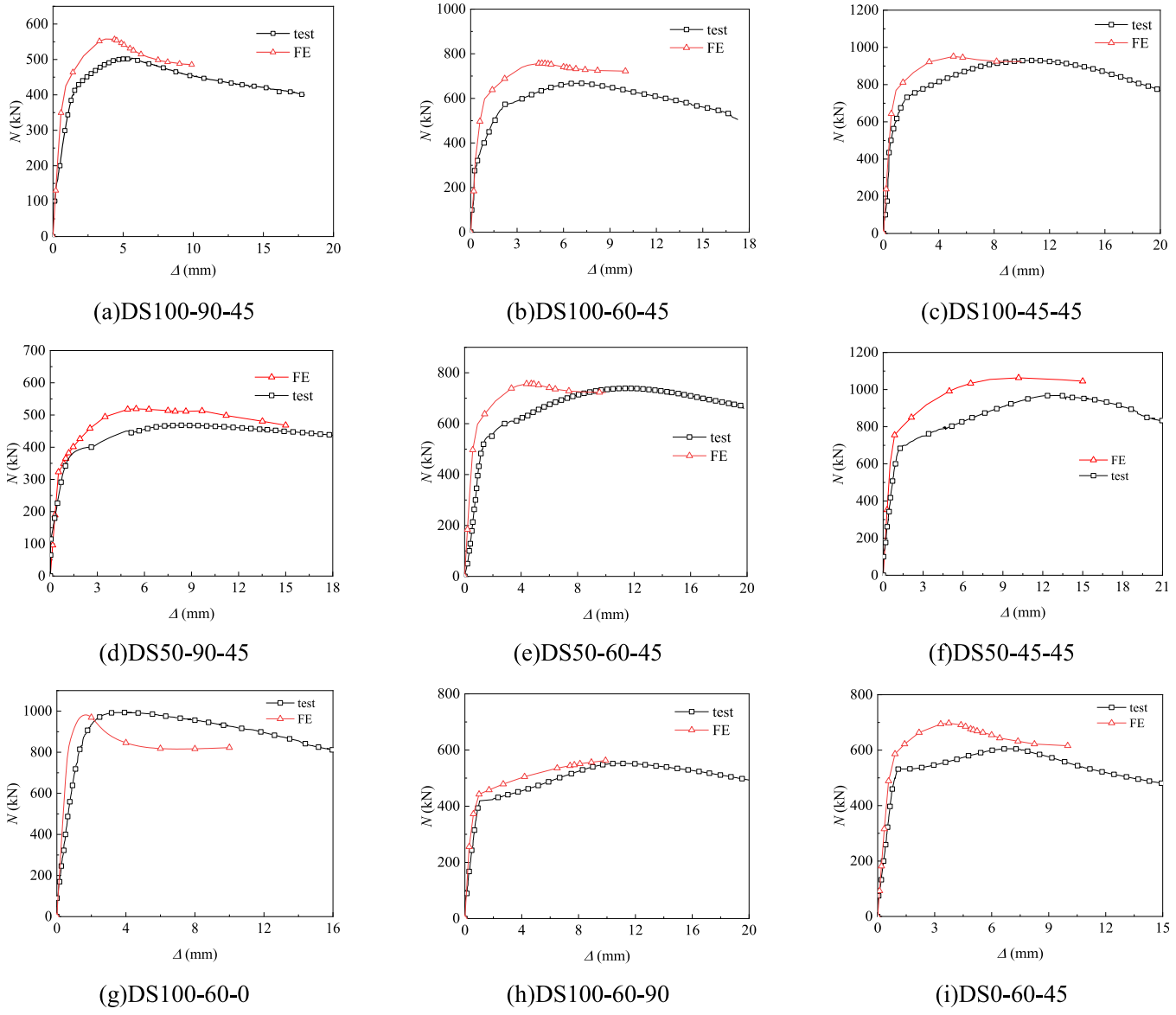

Fig. 15. Validation of the mechanical field model tested in this paper.

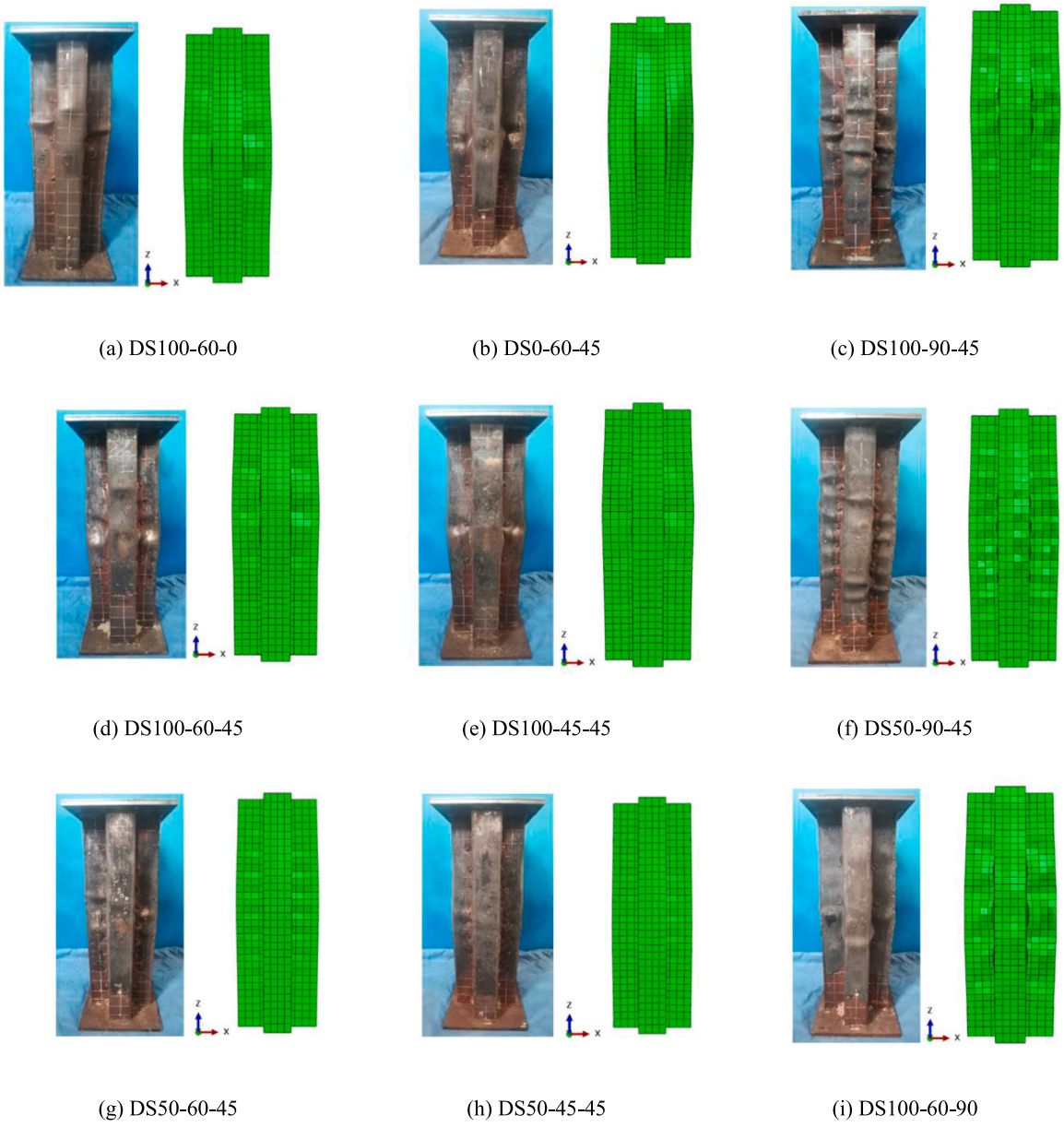

(a) DS100-60-0 (b) DS0-60-45 (c) DS100-90-45

(d) DS100-60-45 (e) DS100-45-45 (f) DS50-90-45

(g) DS50-60-45 (h) DS50-45-45 (i) DS100-60-90

Fig. 16. Failure mode of cross-shaped stiffened concrete-filled steel tubular stub columns after fire exposure.

spacing between stiffeners S were used for parameter analysis. The sectional parameters of the member are shown in Fig. 1, the height of the specimen is taken as three times the limb width and the values of each parameter are provided in Table 6.

5.1. Parametric analysis

5.1.1. Influence of each parameter on the residual bearing capacity

The influence of various parameters on the residual bearing capacity of cross shaped stiffened steel tube concrete stub columns is shown in Fig. 17. As can be seen from the figure, the residual bearing capacity of the member decreases with the increase in heating time t_h and the longitudinal spacing between stiffeners S. The effect of heating time on the residual bearing capacity of members is significant. For example, taking a stiffener spacing of 100 mm, the residual bearing capacity of specimens with heating times of 30 min, 60 min, and 90 min decreased by 6.1 %, 25.48 %, and 35.48 % compared to unfired specimens.

The residual bearing capacity of the member increases with the steel tube thickness, concrete strength, steel tube yield strength, limb thickness, and section size. Among these factors, the improvement of limb thickness b is most significant. For example, with a heating time of 30 min, and keeping the limb width/thickness constant at three,

Table 6
Parameter Values.

Parameter	Values	Default	Parameter	Values	Default
t_h (min)	0,30,60,90		h/b	2,2.5,3,3.5,4	3
f_{cu}(MPa)	30,40,50,60	40	b (mm)	60,8100,120	80
f_y (MPa)	235,345,390,420	345	S (mm)	-,50,10,150	100
t_s (mm)	2,3,4,5	3	f_{yb} (MPa)	335,400,500	335

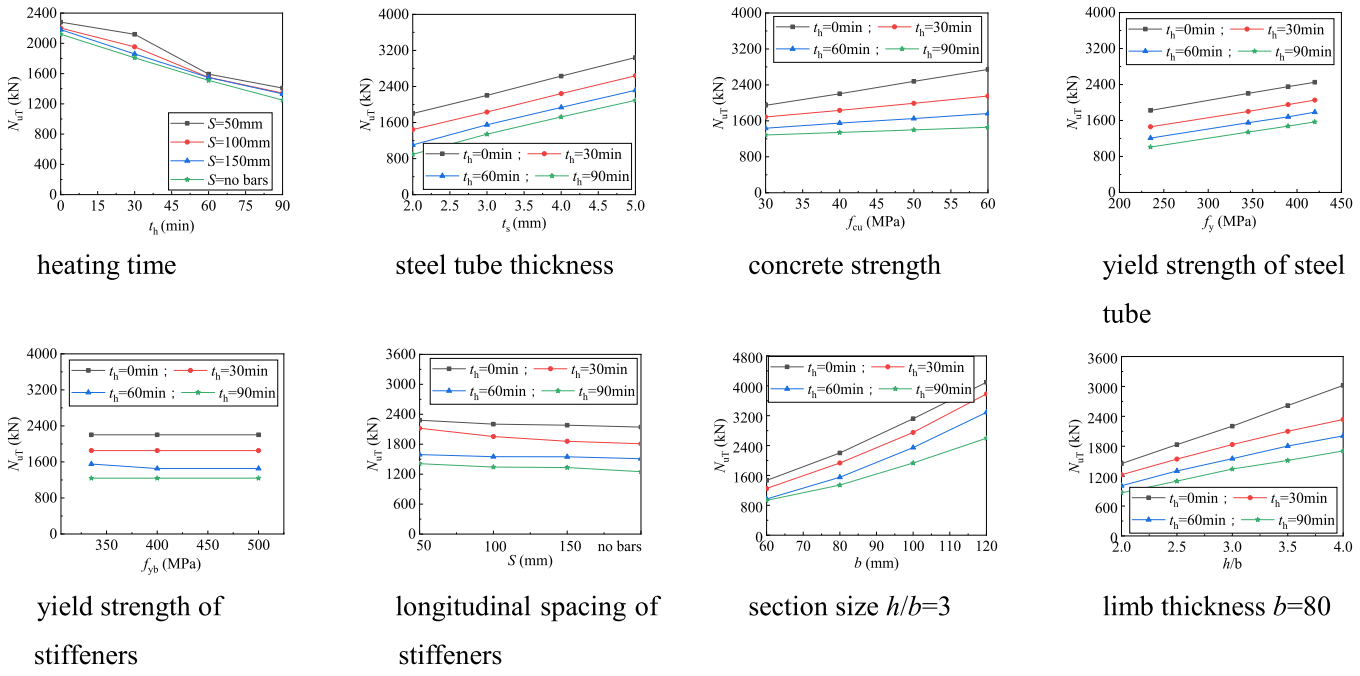

Fig. 17. Effect of various parameters on residual bearing capacity.

increasing the limb thickness from 60 mm to 80 mm, 100 mm, and 120 mm, results in the increases in residual bearing capacity by 46.6 %, 136 %, and 218 %, respectively. However, the changes in the yield strength of steel stiffeners and the longitudinal spacing between stiffeners have little effect on the improvement of the residual bearing capacity of the member.

5.1.2. Influence of each parameter on the reduction coefficient of residual bearing capacity

The ratio of residual bearing capacity after fire, N_{uT}, to ultimate bearing capacity at room temperature, N_u, is the reduction coefficient of residual bearing capacity k_{cr}:

$$k_{cr} = N_{uT}/N_u \quad (2)$$

The influence of the reduction coefficient of residual bearing capacity of the member after fire exposure in relation to various parameters is shown in Fig. 18. It can be seen that the reduction coefficient of residual bearing capacity of members decreases with the increase in heating time, concrete strength, and section size. For example, with the longitudinal spacing of stiffeners of 100 mm, the reduction coefficients of specimens with heating time of 30 min, 60 min, and 90 min are 0.113, 0.296, and 0.391 lower than those of specimens not exposed to fire, respectively. Moreover, the concrete strength increased from C30 to C60, and the reduction coefficients decreased by 0.262, 0.296, 0.334, and 0.358, respectively. As section size h/b increases from 2 to 4, the

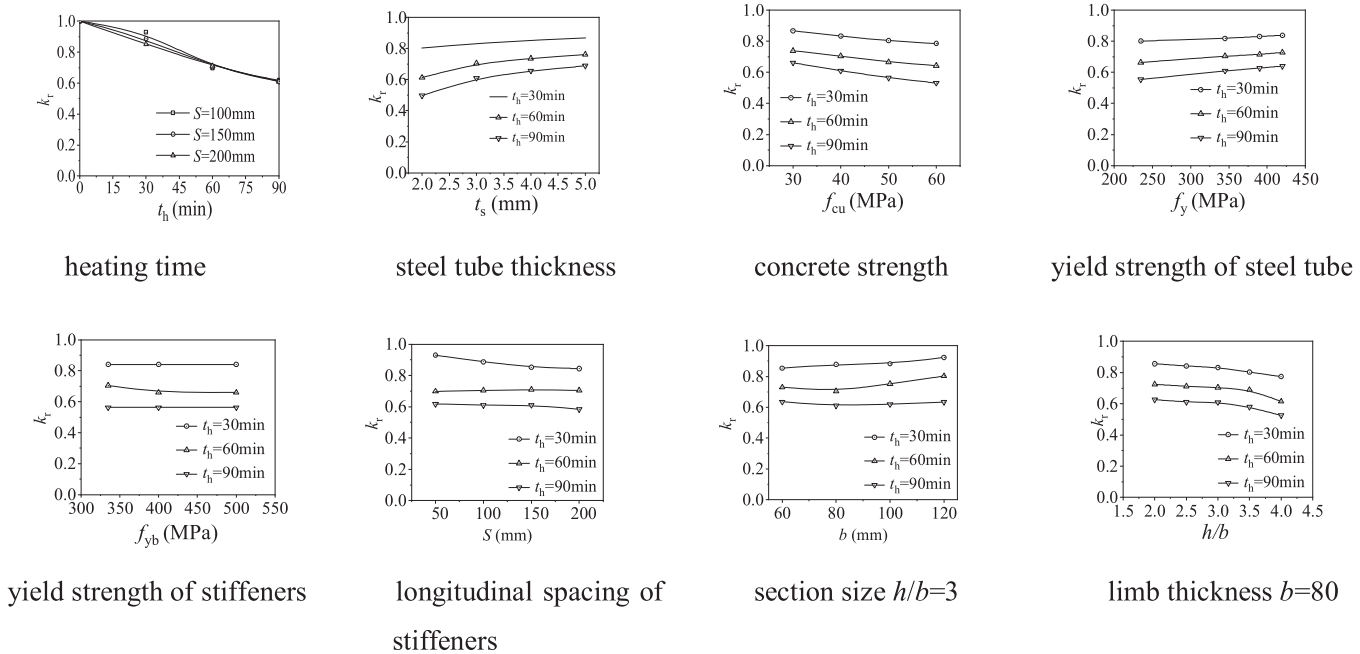

Fig. 18. The influence of each parameter on the reduction coefficient of residual bearing capacity.

reduction coefficients decrease by 0.275, 0.289, 0.296, 0.321, and 0.385, respectively.

The reduction coefficient of residual bearing capacity increases with the increase in steel tube thickness, the yield strength of the steel tube, and limb thickness. Taking the heating time of 60 min as an example, when the steel tube thickness increases from 2 mm to 5 mm, the reduction coefficient decreases by 0.388, 0.296, 0.265 and 0.239, respectively. When the yield strength of the steel tube increases from Q235 to Q420, the reduction coefficients decrease by 0.337, 0.296, 0.285, and 0.272, respectively. Moreover, when the limb thickness increases from 60 mm to 120 mm, the reduction coefficients decrease by 0.271, 0.296, 0.248, and 0.197, respectively. The steel stiffener rib yield strength and the longitudinal spacing of stiffeners have little effect on the reduction coefficient of residual bearing capacity of components after fire.

5.2. Calculation method

5.2.1. Ultimate bearing capacity at room temperature

A simplified approach for calculating the axial bearing capacity of CSCFST stub columns, following Chen et al·[50], is presented below:

$$N_u = \phi_1 f_{ay} A_1 + \phi_2 f_{ay} A_2 + \phi_c f_{ck} A_c \tag{3}$$

where, ϕ_1,$\phi_2$are the strength conversion coefficients of the cross-shaped concrete filled steel tube side plates and end plates respectively. (See Fig. 1 for the cross-shaped specimen side plates corresponding to a_1 and b_1 steel tubes. The end plate corresponds to the a_2, b_2 parts of the steel tube). ϕ_c is the improvement coefficient of concrete; f_{ay} is the yield strength of steel tube. A_1,A_2 are the section areas of the side plate and the end plate respectively. f_{ck} is the compressive strength of concrete and A_c is the concrete section area. Through experimental research, the calculation formulas for the conversion coefficients of side plate and end plate as well as the improvement coefficient of ϕ_1,ϕ_2,$\phi_c$were regressed, as shown in formulas (4) to (9):

$$\phi_1 = \begin{cases} 0.89 & R_1 < 0.85 \\ \dfrac{1.2}{R_1} - \dfrac{0.3}{{R_1}^2} & R_1 \geq 0.85 \end{cases} \tag{4}$$

$$\phi_2 = \begin{cases} 0.89 & R_2 < 0.85 \\ \dfrac{1.2}{R_2} - \dfrac{0.3}{{R_2}^2} & R_2 \geq 0.85 \end{cases} \tag{5}$$

$$\phi_c = 0.2359\overline{R}^{-0.7975}\left(0.721 + 0.9145\zeta^{0.3281}\right)(2.0847 + 0.1253K) \tag{6}$$

$$\text{effective width to thickness } \overline{R} = \sqrt{R_1 R_2} \tag{7}$$

$$\text{constraint coefficient of the stiffener } \zeta = \frac{f_y A_s}{f_{ck} a_s b_s} \tag{8}$$

$$\text{Section shape coefficient } K = \frac{a_1}{b_2} \tag{9}$$

where, R_1 and R_2 are the width to thickness ratio parameters of the side plate steel tube and the end plate steel tube, respectively, which are calculated according to Eq. (10). f_y is the yield strength of the stiffener.A_s is the cross-sectional area of the stiffener. $a_s$and $b_s$are the transverse and longitudinal spacing of the stiffener respectively. $a_1$and $b_2$are the widths of the side plate and the end plate respectively.

$$R_i = \frac{B_i}{t_i}\sqrt{\frac{12(1-\nu^2)}{4\pi^2}}\sqrt{\frac{f_{ay}}{E_s}} \tag{10}$$

where, $B_i$and t_i are width and thickness of the i-th side of steel tube respectively. ν is the Poisson's ratio of the steel tube and E_s is the elastic modulus of the steel tube.

Due to the equal length of the side and end plates in the specimens, and the use of equal limbs in the cross-section, a simplified calculation formula suitable for the cross shaped reinforced steel tube concrete stub column in this paper at room temperature is obtained by simplifying the above formula, as shown in Eqs. (11) to (15);

$$N_u = \phi_s f_y A_s + \phi_c f_{ck} A_c \tag{11}$$

where, N_u is the axial compressive bearing capacity of cross shaped reinforced steel tube concrete. $\phi_s$is the strength conversion coefficient of steel plate. ϕ_c is the improvement coefficient of concrete. f_y is the yield strength of steel tube. $A_s$is the cross-sectional area of steel tube. f_{ck} is the compressive strength of concrete, and A_c is the cross-sectional area of concrete.

$$\phi_s = \begin{cases} 0.89 & R < 0.85 \\ \dfrac{1.2}{R} - \dfrac{0.3}{R^2} & R \geq 0.85 \end{cases} \tag{12}$$

$$\phi_c = 0.5213R^{-0.7975}\left(0.721 + 0.9145\zeta^{0.3281}\right) \tag{13}$$

$$R = \frac{b}{t}\sqrt{\frac{12(1-\nu^2)}{4\pi^2}}\sqrt{\frac{f_y}{E_s}} \tag{14}$$

$$\zeta = \frac{f_{yb} A_b}{f_{ck} a_s b_s} \tag{15}$$

where R is the width to thickness ratio parameter. b is the thickness of the limb. t is the thickness of the steel tube. ν is the Poisson's ratio of the steel tube. f_y is the yield strength of steel tube. E_s is the elastic modulus of the steel tube. $\zeta$is constraint coefficient of the stiffener. f_{yb} is the yield strength of the stiffener. A_b is the cross-sectional area of the stiffener. f_{ck} is the compressive strength of concrete. a_s and b_s are the transverse and longitudinal spacing of the stiffener respectively.

5.2.2. Ultimate bearing capacity after fire

On the basis of the calculation formula at ambient temperature and considering the influence of high temperature effect, a simplified calculation method for residual bearing capacity after fire is derived as shown in (16) - (23).

$$N_u(T_{\max}) = \phi_s f_y(T_{\max}) A_s + \phi_c f_{ck}(T_{\max}) A_c \tag{16}$$

$$\phi_s(T_{\max}) = \begin{cases} 0.89 & R(T_{\max}) < 0.85 \\ \dfrac{1.2}{R(T_{\max})} - \dfrac{0.3}{R(T_{\max})^2} & R(T_{\max}) \geq 0.85 \end{cases} \tag{17}$$

$$\phi_c(T_{\max}) = 0.5213R(T_{\max})^{-0.7975}\left(0.721 + 0.9145\zeta(T_{\max})^{0.3281}\right) \tag{18}$$

$$R(T_{\max}) = \frac{b}{t}\sqrt{\frac{12\left(1-\nu(T_{\max})^2\right)}{4\pi^2}}\sqrt{\frac{f_y(T_{\max})}{E_s(T_{\max})}} \tag{19}$$

$$\zeta(T_{\max}) = \frac{f_{yb}(T_{\max}) A_b}{f_{ck}(T_{\max}) a_s b_s} \tag{20}$$

$$f_{yb}(T_{\max}) = (-0.29t_h + 1.0) f_{yb} \tag{21}$$

$$f_{ck}(T_{\max}) = \left[0.385\left(\frac{h}{b}\right)0.478 + 0.242\right]^{t_h} f_{ck} \tag{22}$$

$$f_y(T_{\max}) = \left(0.08t_h^2 - 0.38t_h + 1.0\right) f_y \tag{23}$$

where $N_u(T_{\max})$ is the axial compressive bearing capacity of cross shaped reinforced steel tube concrete after fire; $\phi_s(T_{\max})$,$\phi_c(T_{\max})$,$f_y(T_{\max})$,$f_{ck}(T_{\max})$,$R(T_{\max})$,$\nu(T_{\max})$,$\zeta(T_{\max})$,

$f_{yb}(T_{max})$,$f_{ck}(T_{max})$, these parameter formulas are the same as those under room temperature conditions, except that they are all functions of the maximum temperature the material will withstand.

The comparison between the results obtained from proposed formula and the values obtained from finite element simulation are shown in Fig. 19, which is based on coefficient of determination (R^2) and mean square error (MSE) [51,52]. The R^2 of the two is 0.925 and the MSE is 0.085, indicating that the results of the proposed formula are in good agreement with the simulation values.

6. Conclusions

The experimental research on CSCFST stub columns after a fire was conducted, and the finite element model of the temperature field and mechanical analysis was established using ABAQUS software. Through parameter analysis, a simplified calculation method for bearing capacity after a fire was derived. The main conclusions are as follows:

(1) Steel has higher thermal conductivity than concrete. This difference combined with the heat absorption and heat transfer hysteresis properties of concrete results in steel tubes heating more quickly and achieving higher maximum historical temperatures than concrete. For concrete measuring points with the same cross-section of the same specimen, the closer they are to the fire boundary, the faster their heating rate and the higher their historical maximum temperature. Moreover, the longer the heating time, the higher the historical maximum temperature the specimen can attain. The width-to-thickness ratio and spacing between stiffeners have little effect on the heat transfer of the specimen.

(2) The buckling of the specimen mainly occurs in the middle region of members, and the failure mode is primarily longitudinal crushing failure of concrete. An increase in heating time will reduce the residual bearing capacity and axial compression stiffness of the specimen, but it can significantly improve the ductility of the specimen. A decrease in the width-to-thickness ratio can enhance the residual bearing capacity, axial compression stiffness, and ductility of the specimen. The reduction of stiffener spacing can significantly improve ductility, but it only slightly improves the residual bearing capacity and axial compression stiffness of the specimen.

(3) Considering parameters such as heating time, compressive strength of concrete, yield strength of steel tube, yield strength of steel stiffener, thickness of steel tube, limb thickness, section size, and longitudinal stiffener spacing, the residual bearing capacity of the tested specimens after exposing to fire and its reduction coefficient are analyzed. It is found that, the reduction coefficients of specimens subjected to 30 min, 60 min, and 90 min of heating are 0.113, 0.296, and 0.391 lower, respectively, than those without fire exposure; when the limb thickness increases from 60 mm to 120 mm, the reduction coefficients decrease by 0.271, 0.296, 0.248, and 0.197, respectively. A simplified calculation formula for residual bearing capacity is proposed, and the coefficient of determination of the two is 0.925 and the mean square error is 0.085, indicating that the results of the proposed formula are in good agreement with the simulation values.

In this paper, only the uniform fire mode is considered, whereas the members are sometimes in a non-uniform fire state during an actual fire. Therefore, it is necessary to further conduct experimental research under non-uniform fire conditions. Additionally, experimental studies and theoretical analyses under various coupling effects, such as fire and hysteresis properties, should be further considered in the future.

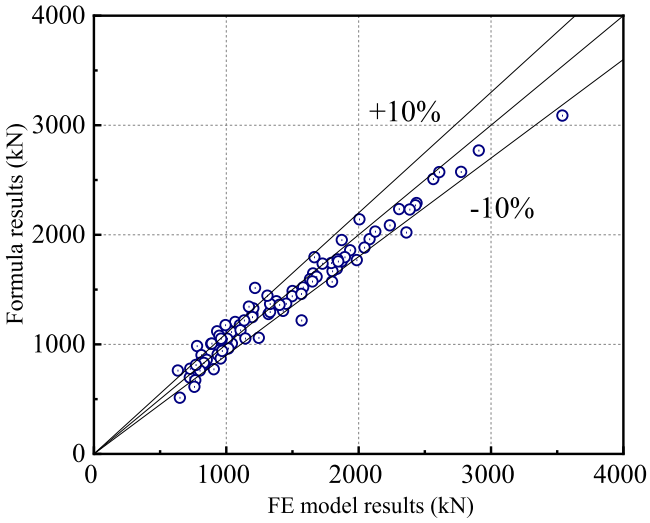

Fig. 19. Comparison of finite element simulation values and formula results.

CRediT authorship contribution statement

Xin Liu: Writing – review & editing, Methodology, Investigation. **Jun Zheng:** Writing – review & editing, Supervision, Resources. **Han Gao:** Writing – review & editing, Software, Investigation. **Yang Yu:** Writing – review & editing, Validation, Software. **Weiwei Wang:** Writing – original draft, Formal analysis, Conceptualization. **Xuetao Lyu:** Writing – review & editing, Supervision, Conceptualization.

Declaration of Competing Interest

The authors declare that they have no known competing financial interests or personal relationships that could have appeared to influence the work reported in this paper.

Acknowledgements

This research was supported by the National Natural Science Foundation of China (51208246) and the Foundation of Key Laboratory of Structures Dynamic Behavior and Control (Ministry of Education) (HITCE202007) in Harbin Institute of Technology. The authors would like to appreciate financial and technical support from funding bodies.

References

[1] Ayough P, Wang YH, Ibrahim Z. Analytical study of concrete-filled steel tubular stub columns with double inner steel tubes. Steel Compos Struct 2023;47:645–61.
[2] Ci J, Ahmed M, Tran VL, Jia H, Chen S, Nguyen TN. Buckling resistance of axially loaded square concrete-filled double steel tubular columns. Steel Compos Struct 2022;43:689–706.
[3] Memarzadeh A, Shahmansouri AA, Poologanathan K. A novel prediction model for post-fire elastic modulus of circular recycled aggregate concrete-filled steel tubular stub columns. Steel Compos Struct 2022;44:309–24.
[4] Mou B, Wang Z, Qiao Q, Zhou W. Exposed Reinforced concrete-filled steel tubular (RCFST) column-base joint with high-strength. Steel Compos Struct 2022;44:1–15.
[5] Zhang B, Wang Y, Li G, Qu S, Fu C, Xu T. Structural performance of steel reinforced concrete T-shaped columns exposure to high temperature. Structures 2021;34:716–28.
[6] Liew JYR, Xiong M, Xiong D. Design of concrete filled tubular beam-columns with high strength steel and concrete. Structures 2016;8:213–26.
[7] Reddy GSR, Bolla M, Patton ML, Adak D. Comparative study on structural behaviour of circular and square section-Concrete Filled Steel Tube (CFST) and Reinforced Cement Concrete (RCC) stub column. Structures 2021;29:2067–81.
[8] Van Cao V, Trinh TMN. Performance of circular concrete filled steel tubes after fire exposure: experiments. Structures 2023;55:1331–41.
[9] Chen H, Wu L, Jiang H, Liu Y. Seismic performance of prefabricated middle frame composed of special-shaped columns with built-in lattice concrete-filled circular steel pipes. Structures 2021;34:1443–57.

[10] Liu X, Liu J, Yang Y, Cheng G, Lanning J. Resistance of special-shaped concrete-filled steel tube columns under compression and bending. J Constr Steel Res 2020;169.
[11] Liu X, Zhang J, Lu H, Guan N, Xiao J, Du G. Behavior of the T-Shaped Concrete-Filled Steel Tubular Columns after Elevated Temperature. Adv Civ Eng 2021:6638736.
[12] Wang FC, Han LH. Analytical behavior of special shaped CFST stub columns under axial compression. Thin-Walled Struct 2018;129:404–17.
[13] Yang Y, Wang Y, Fu F, et al. Static behavior of T-shaped concrete-filled steel tubular columns subjected to concentric and eccentric compressive loads. Thin-Walled Struct 2015;95:374–88.
[14] Li MH, Zong ZH, Hao H, Zhang XH, Lin J, Xie GY. Experimental and numerical study on the behaviour of CFDST columns subjected to close-in blast loading. Eng Struct 2019;185:203–20.
[15] Liang QQ, Liew JYR, Uy Brian. Local buckling of steel plates in concrete-filled thin walled steel tubular beam-columns. J Constr Steel Res 2007;24:396–405.
[16] Wang XT, Xie CD, Lin LH, Li J. Seismic behavior of self-centering concrete filled square steel tubular(CFST) Column Base. J Constr Steel Res 2019;156:75–85.
[17] Meng FQ, Zhu MC, et al. Performance of square steel-reinforced concrete-filled steel tubular columns subject to non-uniform fire. J Constr Steel Res 2020;166:1–10.
[18] Yin F, Xue SD, Cao WL, Dong HY, Wu HP. Experimental and analytical study of seismic behavior of special-shaped multicell composite concrete-filled steel tube columns. J Struct Eng 2020;146:04019170.
[19] Zuo ZL, Cai J, Chen QJ, et al. Performance of T-shaped CFST stub columns with binding bars under axial compression. Thin-Walled Struct 2018;129:183–96.
[20] Yang YL, Wang YY, Fu F. Effect of reinforcement stiffeners on square concrete filled steel tubular columns subjected to axial compressive load. Thin-Walled Struct 2014;82:132–44.
[21] Tao Z, Han LH, Wang DY. Experimental behaviour of concrete-filled stiffened thin-walled steel tubular columns. Thin-Walled Struct 2007;45:517–27.
[22] Hu HS, Fang PP, Liu Y, Guo ZX, Shahrooz BM. Local buckling of steel plates in composite members with tie bars under axial compression. Eng Struct 2020;205:110097.
[23] Lyu XT, Xu Y, Xu Q, Yu Y. Axial compression performance of square thin walled concrete-filled steel tube stub columns with reinforcement stiffener under constant high-temperature. Materials 2019;12:1098.
[24] Xu C, Yang Y, Tang X, et al. Experimental research on static behavior of stiffened T-shaped concrete-filled steel tubular stubs subjected to concentric axial loading. Int J Steel Struct 2019;19:591–602.
[25] Farzad R, Ali A, Armin M, et al. Experimental study of post-fire bond behavior of concrete-filled stiffened steel tubes: A crucial aspect for composite structures. Structures 2024;62:106203.
[26] Venkatachari S, Kodur VKR. Modeling parameters for predicting the fire-induced progressive collapse in steel framed buildings. Resilient Cities Struct 2023;2:129–44.
[27] Ali F, Nadjai A, Choi S. Numerical and experimental investigation of the behavior of high strength concrete columns in fire. Eng Struct 2010;32:1236–43.
[28] Han LH, Huo JS. Concrete-filled hollow structural steel columns after exposure to ISO-834 fire standard. J Struct Eng 2003;129:68–78.
[29] David M, Manuel L, Huu-Tai T, Ana E. Fire design of steel-reinforced CFST stub columns with high-strength materials. J Constr Steel Res 2024;218:108692.
[30] Medall D, Ibáñez C, Albero V, Ana E, et al. Experimental residual capacity of steel-reinforced concrete-filled steel tubular stub columns after fire exposure. Thin-Walled Struct 2023;189:110900.
[31] Meng FQ, Zhu MC, Mou B, He BJ. Residual strength of steel-reinforced concrete-filled square steel tubular (SRCFST) stub columns after exposure to ISO-834 standard fire. Int J Steel Struct 2019;19:850–66.
[32] Liu FQ, Yang H, Wang W. Behaviours of concentrically and eccentrically loaded square steel tube confined reinforced concrete slender columns after fire exposure. Thin-Walled Struct 2021;158:107155.
[33] Thumrongvut J, Tipcharoen A, Prathumwong K. Post-fire performance of square concrete-filled steel tube columns under uni-axial load. Mater Sci Forum 2021;1016:618–23.
[34] Lyu XT, Zhang T, Liu FQ, Liu Y. Behaviours of stiffened concrete-filled thin-walled square steel tubular stub columns after non-uniform fire exposure. J Constr Steel Res 2022;188:107031.
[35] Zhang T, Lyu XT, Liu H, Yu Y, Xu Y. Analysis of finite element mechanism of axial compressive behavior of T-shaped stiffened concrete-filled steel tubular stub columns after uniform fire exposure. Int J Steel Struct 2021;21:836–49.
[36] Lyu XT, Li Y, Li H, Wang WW, Liu FQ, Xu Y. Behaviour of T-shaped stiffened concrete-filled steel tubular stub columns after uniform and non-uniform fire exposure. Adv Struct Eng 2023;0:1–13. https://doi.org/10.1177/13694332231214999.
[37] Lyu XT, Wang WW, Li H, Li JH, Yu Yang. Numerical and experimental analysis on the axial compression performance of T-shaped concrete-filled thin-walled steel tubular long columns after fire exposure. Steel Compos Struct 2024;50:383–401.
[38] Wang WW, Lyu XT, Zhang YZ, Yu Y, Zhang T. Axial compression performance of thin-walled T-shaped concrete filled steel tubular columns under constant high temperature: Experimental and numerical study. Structures 2020;27:525–41.
[39] GB/T228.1–2010. Metallic materials-Tensile testing-Part 1: Method of test at room temperature. National Standards of the People's Republic of China; 2010.
[40] GB/T50081–2002. Standard for Test Method of Mechanical Properties on Ordinary Concrete. National Standards of the People's Republic of China; 2002.
[41] GB/T20313–2006. Hygrothermal performance of building materials and produts-Determinaton of moisture content by drying at elevated temperature. National Standards of the People's Republic of China; 2006.
[42] Eurocode 4, 2004. Design of composite steel and concrete structures, part1: general rules-structural fire design[S]. ENV 1994–1-2:2004, European Committee for Standardization, Brussels.
[43] Lyu XT, Yang H, Zhang SM. Effect of contact thermal resistance on temperature distribution of concrete-filled steel tubes in fire. J Harbin Inst Technol(N Ser) 2011;18:99–106.
[44] Tao Z, Wang XQ, Uy Brian. Stress-Strain Curves of Structural and Reinforcing Steels after Exposure to Elevated Temperatures[J]. J Mater Civ Eng 2013;25(9):1306–16.
[45] American Concrete Institute. Building code requirements for structural concrete (ACI 318–11) and commentary. Farmington Hills, MI, USA; 2011.
[46] Xie D, Qian Z. Experimental study on strength and deformation of concrete under high temperature(open fire). Eng Mech 1996;S1:54–8.
[47] Han LH, Yang Y, Yang H, et al. Residual strength of concrete-filled RHS columns after exposure to the ISO-834 standard fire. Thin Walled Struct 2002;40:991–1012.
[48] Hong S, Varma AH. Analytical modeling of the standard fire behavior of loaded CFT columns. J Constr Steel Res 2009;65:54–69.
[49] Liu FQ, Yang H, Yan R, Wang W. Experimental and numerical study on behaviour of square steel tube confined reinforced concrete stub columns after fire exposure. Thin-Walled Struct 2019;139:105–25.
[50] Chen QG, Cai J, Zuo ZL, Huang JX, Wei JY. Study on cross-shaped concrete filled steel tubular stub columns subjected to axial compression: experiments and design method. Open Civ Eng J 2017;11:1–13.
[51] Yu Y, Zhang C, Xie X, Yousefi AM, Zhang G, Li J, Samali B. Compressive strength evaluation of cement-based materials in sulphate environment using optimized deep learning technology. Dev Built Environ 2023;16:100298.
[52] Yu Y, Hoshyar AN, Samali B, Zhang G, Rashidi M. Masoud M. Corrosion and coating defect assessment of coal handling and preparation plants (CHPP) using an ensemble of deep convolutional neural networks and decision-level data fusion. Neural Comput Appl 2023;35(25):18697–718.